


Article

Nonlinear Optical Potential with Parity-Time Symmetry in a Coherent Atomic Gas

Delvi Antonio Polanco Adames ¹, Jianpeng Dou ², Ji Lin ¹, Gengjun Zhu ¹ and Huijun Li ^{1,*} 

¹ College of Physics and Electronic Information Engineering, Zhejiang Normal University, Jinhua 321004, China; delvipolanco2017@gmail.com (D.A.P.A.); linji@zjnu.edu.cn (J.L.); gjzhu@zjnu.cn (G.Z.)

² Department of Physics and Astronomy, Shanghai Jiao Tong University, Shanghai 200240, China; doujianpeng@sjtu.edu.cn

* Correspondence: hjli@zjnu.cn

Abstract: We propose a scheme to realize a parity-time (\mathcal{PT}) symmetric nonlinear system in a coherent atomic gas via electromagnetically induced transparency. We show that it is possible to construct an optical potential with \mathcal{PT} symmetry due to the interplay among the Kerr nonlinearity stemmed from the atom-photon interaction, the linear potential induced by a far-detuned Stark laser field, and the optical gain originated from an incoherent pumping. Since the real part of the \mathcal{PT} -symmetric potential depends only on the intensity of the probe field, the potential is nonlinear and its \mathcal{PT} -symmetric properties are determined by the input laser intensity of the probe field. Moreover, we obtain the fundamental soliton solutions of the system and attain their stability region in the system parameter space. The dependence of the exceptional point (EP) location on the soliton maximum amplitude is also illustrated. The research results reported here open a new avenue for understanding the unique properties of \mathcal{PT} symmetry of a nonlinear system. They are also promising for designing novel optical devices applicable in optical information processing and transmission.

Keywords: parity-time symmetry; electromagnetically induced transparency; soliton



Citation: Polanco Adames, D.A.; Dou, J.; Lin, J.; Zhu, G.; Li, H. Nonlinear Optical Potential with Parity-Time Symmetry in a Coherent Atomic Gas. *Symmetry* **2022**, *14*, 1135. <https://doi.org/10.3390/sym14061135>

Academic Editors: Wu-Ming Liu and Xingdong Zhao

Received: 14 April 2022

Accepted: 26 May 2022

Published: 31 May 2022

Publisher's Note: MDPI stays neutral with regard to jurisdictional claims in published maps and institutional affiliations.



Copyright: © 2022 by the authors. Licensee MDPI, Basel, Switzerland. This article is an open access article distributed under the terms and conditions of the Creative Commons Attribution (CC BY) license (<https://creativecommons.org/licenses/by/4.0/>).

1. Introduction

The inherent loss of a practical physical system usually brings the non-Hermiticity of Hamiltonian, making the system an open one, and leads to a complex eigen spectrum. Surprisingly, a special class of non-Hermitian Hamiltonians with parity-time (\mathcal{PT}) symmetry may have an entire real spectrum [1,2] in a definite parameter range. Thanks to the mathematical equivalence between the Schrödinger equation in quantum mechanics and the Maxwell equation under paraxial approximation in optics, the concept of \mathcal{PT} symmetry was soon introduced into the content of optics [3–13]. In optics, \mathcal{PT} symmetry indicates that the real part of a complex optical potential $V(\mathbf{r})$ is an even function of space while its imaginary part is an odd function, i.e., $V(\mathbf{r}) = V^*(-\mathbf{r})$. Particularly, there is a critical threshold, alias as the exceptional point (EP), at which the system experiences a phase transition from the \mathcal{PT} symmetry to the broken \mathcal{PT} symmetry. If the \mathcal{PT} -symmetric system is a linear one, the location of EP is determined by the ratio between the imaginary and real parts of the \mathcal{PT} -symmetric potential, which is irrelevant to the intensity of the input laser field. In this case, when the system works in the unbroken \mathcal{PT} -symmetric phase, all eigenvalues are real and the corresponding eigenmodes of the system are stable; on the other hand, when the system works in the broken \mathcal{PT} -symmetric phase, some of eigenvalues become complex and the corresponding eigenmodes are unstable. If the \mathcal{PT} -symmetric system is a nonlinear one, the situation can be very different. In this case, the location of EP is closely related to the intensity of the input laser field. This is because the Kerr nonlinearity can be treated as a part of the optical potential, which can eventually modify the ratio between the imaginary and real parts of the potential.

In recent years, many intriguing phenomena and important applications have been shown and suggested for optical \mathcal{PT} -symmetric systems, including the loss induced

transparency [9], coherent perfect absorbers [10], unidirectional light propagation [6], unidirectional invisibility [5,14], nonreciprocal light propagation [7,8], single-mode microring lasers [15,16], enhanced sensing [17,18], and so on. However, most of above phenomena were studied only for the linear systems. Therefore, it is very interesting to see what will happen when the \mathcal{PT} -symmetric systems are nonlinear. It is also important to note that compared with solid-state materials [3–13], atomic gases are more advantageous in realization of \mathcal{PT} -symmetric structures due to the configurable refractive index profiles, leading to active control of the gain, absorption, and Kerr nonlinearities [19–21].

In this article, we propose a scheme to realize a \mathcal{PT} -symmetric nonlinear system in a coherent atomic gas via electromagnetically induced transparency (EIT). The system under study consists of a cold three-level atomic gas interacting with two lasers. We show that by carefully tuning the Kerr nonlinearity stemmed from the atom-photon interaction, the linear potential induced by a far-detuned Stark laser field, and the optical gain originated from an incoherent pumping between the ground and excited levels, it is possible to construct an optical potential with \mathcal{PT} symmetry. In contrast with previous studies, the real part of the \mathcal{PT} -symmetric potential in the present system depends only on the intensity of the probe field through the Kerr nonlinear effect. Therefore, the \mathcal{PT} -symmetric potential is a nonlinear one and its \mathcal{PT} -symmetric properties are determined by the input laser intensity of the probe field. Moreover, we obtain the fundamental soliton solutions of the system and find their stability region in the system parameter space. Finally, we illustrate that the EP location can be changed and actively controlled by tuning the soliton amplitude. The research results reported here is not only useful for understanding the unique properties of \mathcal{PT} symmetry of a nonlinear optical potential, but also promising for designing novel optical devices applicable in optical information processing and transmission.

2. Model and the Motion Equation for the Scheme

2.1. Model

We consider a cold ^{87}Rb atomic gas with Λ -type energy state, see Figure 1. The energy levels are chosen from D₁ line of ^{87}Rb , here $|1, 2\rangle = |5S_{1/2}, F = 1, 2\rangle$, and $|3\rangle = |5P_{1/2}, F = 1\rangle$. A weak probe and a strong control light fields $\mathbf{E}_{p,c} = \mathbf{e}_x \mathcal{E}_{p,c}(x, z, t) \exp[i(k_{p,c}z - \omega_{p,c}t)] + \text{c.c.}$ interact near resonantly with energy levels $|1\rangle \rightarrow |3\rangle$ and $|2\rangle \rightarrow |3\rangle$, respectively. Here \mathbf{e}_j and k_j (\mathcal{E}_j) denote respectively the polarization unit vector along the j th direction and the wave number (envelope) of the j th field, and \mathcal{E}_c is constant. The energy levels $|l\rangle$ ($l = 1 - 3$) and $\mathbf{E}_{p,c}$ constitute the well-known Λ -type EIT system.

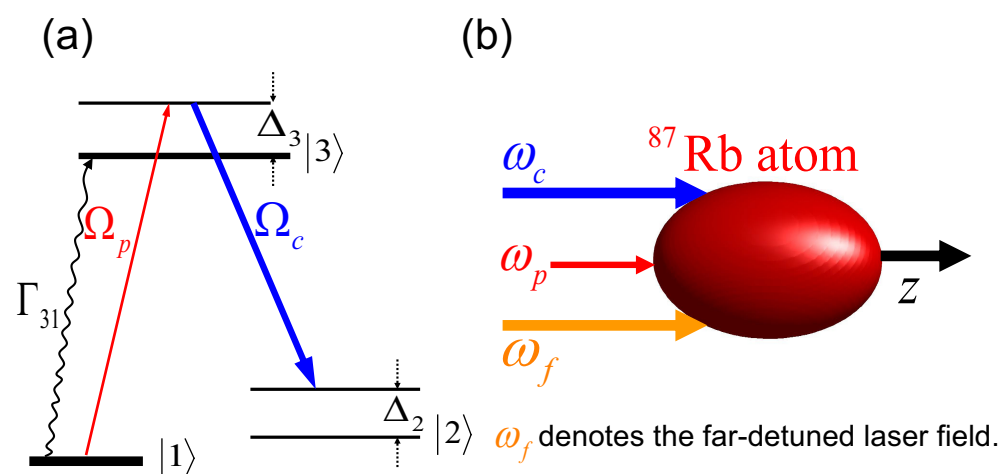


Figure 1. (a) Energy level diagram used to obtain a \mathcal{PT} -symmetric model. (b) A possible experimental setup. All symbols can be found in the text.

In addition, another far-detuned standing-wave Stark field is introduced into the system, reading

$$\mathbf{E}_{\text{Stark}} = \mathbf{e}_y \sqrt{2} E_s(x) \cos(\omega_f t), \quad (1)$$

where $E_s(x)$ and ω_f are the amplitude and angular frequency. Consequently, an x -dependent Stark energy shift of E_j appears, i.e., $E_j \rightarrow E_j + \Delta E_j$, where $\Delta E_j = -\frac{1}{2} \alpha_j \langle \mathbf{E}_{\text{Stark}}^2 \rangle_t = -\frac{1}{2} \alpha_j |E_s(x)|^2$, with α_j the scalar polarizability and $\langle \cdots \rangle_t$ the average in an cycle. The concrete form of $E_s(x)$ will be selected according to the \mathcal{PT} -symmetric requirement (see Section 3).

In order to obtain a gain for the probe light field, which is required by the condition of \mathcal{PT} symmetry, an incoherent optical pumping is also introduced in the system. It pumps atoms from the energy level $|1\rangle$ to the energy level $|3\rangle$ with the pumping rate Γ_{31} as shown in Equations (A1) and (A3) of Appendix A. This kind of pumping has been realized in intense atomical resonant lines emitted from the hollow-cathode lamps or from the microwave discharge lamps [22].

In Figure 1a, $\Omega_p = (\mathbf{e}_x \cdot \mathbf{p}_{13}) \mathcal{E}_p / \hbar$ and $\Omega_c = (\mathbf{e}_x \cdot \mathbf{p}_{23}) \mathcal{E}_c / \hbar$ are respectively the half Rabi frequencies of the probe and control fields, where \mathbf{p}_{ij} is the electric dipole matrix element from $|i\rangle$ to $|j\rangle$ and $\Delta_{3,2}$ are the one- and two-photon detunings, respectively. A possible experimental setup is plotted in Figure 1b.

2.2. Maxwell-Bloch Equations

Under the electric dipole and rotating wave approximations, the Hamiltonian in the interaction picture reads $\hat{H}_{\text{int}} = -\hbar \sum_{j=1}^3 \Delta'_j |j\rangle \langle j| - \hbar (\Omega_p |3\rangle \langle 1| + \Omega_c |3\rangle \langle 2| + \text{h.c.})$, where h.c. denotes Hermitian conjugate, and

$$\Delta'_j = \Delta_j + \frac{\alpha_j}{2\hbar} |E_s|^2. \quad (2)$$

The Bloch equations, describing the motion of atoms, are given by

$$\frac{\partial \rho}{\partial t} = -\frac{i}{\hbar} [\hat{H}_{\text{int}}, \rho] - \Gamma \rho, \quad (3)$$

where ρ is a 6×6 density matrix with the density matrix element ρ_{ij} ($i, j = 1, 2, 3$), and

$$\Gamma = \begin{pmatrix} -\Gamma_{31} & 0 & \Gamma_{13} & 0 & 0 & 0 \\ 0 & 0 & \Gamma_{23} & 0 & 0 & 0 \\ \Gamma_{31} & 0 & -\Gamma_3 & 0 & 0 & 0 \\ 0 & 0 & 0 & \gamma_{21} & 0 & 0 \\ 0 & 0 & 0 & 0 & \gamma_{31} & 0 \\ 0 & 0 & 0 & 0 & 0 & \gamma_{32} \end{pmatrix}, \quad (4)$$

$\gamma_{jl} = (\Gamma_j + \Gamma_l)/2 + \gamma_{jl}^{\text{dph}}$ ($jl \neq 31$), $\gamma_{31} = (\Gamma_3 + \Gamma_{31})/2 + \gamma_{31}^{\text{dph}}$, and $\Gamma_l = \sum_{E_j < E_l} \Gamma_{jl}$. Here γ_{jl}^{dph} denotes the dephasing rates caused by atomic collisions, which can be neglect when the temperature of atoms is low, Γ_{jl} is the rate at which population decays from $|l\rangle$ to $|j\rangle$. Especially, Γ_{31} is the incoherent pumping rate from $|1\rangle$ to $|3\rangle$. The explicit form of the equations of motion for ρ_{ij} is given in Appendix A.

The evolution of the probe field is described by Maxwell equation, which, under the slowly varying amplitude approximation, is given by

$$i \left(\frac{\partial}{\partial z} + \frac{1}{c} \frac{\partial}{\partial t} \right) \Omega_p + \frac{c}{2\omega_p} \frac{\partial^2}{\partial x^2} \Omega_p + \kappa_{13} \rho_{31} = 0, \quad (5)$$

where $\kappa_{13} = N\omega_p |\mathbf{e}_p \cdot \mathbf{p}_{13}|^2 / (2\epsilon_0 \hbar c)$, with N the atomic concentration. In addition, for deriving Equation (5), we have assumed that the probe beam is enough wide in the y direction so that a diffraction term in the y direction (the term $\propto \partial^2 \Omega_p / \partial y^2$) can be safely neglected.

3. Realization of \mathcal{PT} -Symmetric Potential

3.1. The Probe Field Envelope Equation

In order to solve the probe field from Equation (5), one need to obtain the solution of ρ_{31} , firstly, by solving Equations (A1)–(A6). Further, we neglect all derivative with respect to time in the Maxwell-Bloch (MB) Equations (3) and (5) since we are only interested in the stationary states [23,24].

Since the probe field is much weaker than the control field, we employ the method of multiple scales by introducing the expansions $\rho_{ij} = \rho_{ij}^{(0)} + \epsilon \rho_{ij}^{(1)} + \epsilon^2 \rho_{ij}^{(2)} + \epsilon^3 \rho_{ij}^{(3)} + \dots$, $\Omega_p = \epsilon \Omega_p^{(1)} + \epsilon^2 \Omega_p^{(2)} + \epsilon^3 \Omega_p^{(3)} + \dots$, $E_s(x) = \epsilon E_s^{(1)}(x)$, $d_{ij} = d_{ij}^{(0)} + \epsilon^2 d_{ij}^{(2)}$. For avoiding the divergence at each order, we also introduce the multiple scale variables $z_l = \epsilon^l z$ ($l = 0, 1, 2$) and $x_1 = \epsilon x$ [23,24]. Here, ϵ is a small quantity, determined for example by $\epsilon = \Omega_{p,\max}/\Omega_c$. Substituting the expansions into Equations (3) and (5), a sets of equations for $\rho_{ij}^{(l)}$ and $\Omega_p^{(l)}$ ($l = 0, 1, 2, 3, \dots$) are obtained, and can be solved order by order.

At the zeroth order ($\mathcal{O}(\epsilon^0)$ -order), we obtain the base state solutions of the system

$$\rho_{11}^{(0)} = \frac{2\gamma_{32}\Gamma_{13}|\Omega_c|^2}{D_0}, \quad (6)$$

$$\rho_{22}^{(0)} = \frac{2\gamma_{32}\Gamma_{31}|\Omega_c|^2 + \Gamma_{31}\Gamma_{23}|d_{32}^{(0)}|^2}{D_0}, \quad (7)$$

$$\rho_{33}^{(0)} = \frac{2\gamma_{32}\Gamma_{31}|\Omega_c|^2}{D_0}, \quad (8)$$

$$\rho_{32}^{(0)} = -\frac{\Gamma_{23}\Gamma_{31}\Omega_c(d_{32}^{(0)})^*}{D_0}, \quad (9)$$

with other $\rho_{ij}^{(0)} = 0$, and $D_0 = \Gamma_{31}\Gamma_{23}|d_{32}^{(0)}|^2 + 2\gamma_{32}(\Gamma_{13} + 2\Gamma_{31})|\Omega_c|^2$.

At the first order ($\mathcal{O}(\epsilon)$ -order), the solutions are given by $\Omega_p^{(1)} = F(x_1, z_1, z_2) e^{iKz_0}$, $\rho_{21,31}^{(1)} = \alpha_{21,31}^{(1)} e^{iKz_0}$ (the explicit expressions of $\alpha_{21,31}^{(1)}$ are given in Appendix B), with other $\rho_{ij}^{(1)} = 0$. Here, the wavenumber K is given by

$$K = \kappa_{13} \frac{\Omega_c(\rho_{32}^{(0)})^* + d_{21}^{(0)}(\rho_{11}^{(0)} - \rho_{33}^{(0)})}{D_1}, \quad (10)$$

where $D_1 = |\Omega_c|^2 - d_{21}^{(0)}d_{31}^{(0)}$. From the above equation, we see that K is a complex number, with the real (imaginary) part of K representing the dispersion (gain or loss) of the probe field.

Figure 2 gives the imaginary part of K as a function of Δ_3 . From this figure, there is a absorption peak when $\Delta_3 = 0$ in the absence of the control field and the incoherent pumping. However, a typical transparency window is opened when $\Omega_c = 6 \times 10^7$ Hz and $\Gamma_{31} = 0$. But a small abortion $\text{Im}(K) = 0.001 \text{ cm}^{-1}$ still exists when $\Delta_3 = 0$. After introducing the incoherent pumping, a gain appears as shown by the dashed-dotted line in Figure 2 and its inset. Such a gain is necessary for the realization of \mathcal{PT} -symmetric potential of the probe field. Here, the system parameters are taken as $\gamma_1 = \Delta_1 = 0$, $2\gamma_2 = 1 \times 10^3$ Hz, $2\gamma_3 = \Gamma_3 = 36$ MHz, and the tunable parameter $\kappa_{13} = 1.0 \times 10^{10} \text{ cm}^{-1}\text{s}^{-1}$.

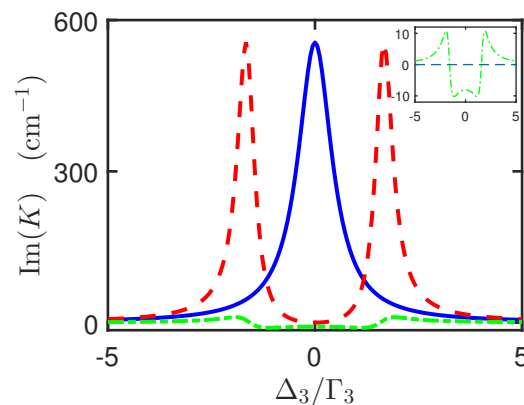


Figure 2. The imaginary part $\text{Im}(K)$ as a function of Δ_3/Γ_3 for $\Delta_2 = \Delta_3$. Solid (blue), dashed (red), and dashed-dotted (green) lines correspond to $(\Omega_c, \Gamma_{31}) = (0, 0)$, $(6 \times 10^7 \text{ Hz}, 0)$, and $(6 \times 10^7 \text{ Hz}, 0.48 \Gamma_3)$, respectively. For a better illustration, the dashed-dotted (green) line has been shown in the inset.

At the second order ($\mathcal{O}(\epsilon^2)$ -order), we find the equation $\frac{\partial F}{\partial z_1} = 0$ and the solutions $\Omega_p^{(2)} = \rho_{21}^{(2)} = \rho_{31}^{(2)} = 0$, and $\rho_{ij}^{(2)} = \alpha_{ij}^{(2)}|F|^2$ ($ij = 11, 22, 33, 32$; $\alpha_{ij}^{(2)}$ are given in Appendix B).

The nonlinear envelope equation of the probe field can also be derived at the third order ($\mathcal{O}(\epsilon^3)$ -order). After returning original variables, the equation reads

$$i\frac{\partial \Omega_p}{\partial z} + \frac{c}{2\omega_p} \frac{\partial^2 \Omega_p}{\partial x^2} + \tilde{V}(x)\Omega_p = 0 \quad (11)$$

with the potential

$$\tilde{V}(x) = W_1|\Omega_p|^2 + W_2|E_s(x)|^2 + K, \quad (12)$$

where $\Omega_p = \epsilon F \exp(iKz)$, $W_1 = \kappa_{13}[\Omega_c(\alpha_{32}^{(2)})^* - d_{21}^{(0)}(\alpha_{33}^{(2)} - \alpha_{11}^{(2)})]/D_1$, and $W_2 = \kappa_{13}[(\alpha_3 - \alpha_1)d_{21}^{(0)}\alpha_{31}^{(1)} - (\alpha_2 - \alpha_1)\Omega_c\alpha_{21}^{(1)}]/(2\hbar D_1)$.

For convenience, Equation (11) can be converted into the dimensionless form

$$i\frac{\partial u}{\partial s} + \frac{\partial^2 u}{\partial \xi^2} + V(\xi)u = 0, \quad (13)$$

with

$$V(\xi) = g_1|u|^2 + g_2|v|^2 + ig_3, \quad (14)$$

where $u = \Omega_p \exp(-i\text{Re}(K)z)/\Omega_{p0}$, $v = E_s/E_{s0}$, $s = z/L_{\text{diff}}$, $\xi = x/R$, $g_1 = W_1\Omega_{p0}^2 L_{\text{diff}}$, $g_2 = W_2 E_{s0}^2 L_{\text{diff}}$, and $g_3 = L_{\text{diff}} \text{Im}(K)$. Here, $L_{\text{diff}} \equiv 2\omega_p R^2/c$ is the characteristic diffraction length, Ω_{p0} is the typical Rabi frequency of the probe field, and E_{s0} denotes the typical amplitude of the far-detuned laser field. Consequently, the probe-field susceptibility is $\chi(x) = 2c\tilde{V}(x)/\omega_p$, and the nonlinear refractive index $n(x) = \sqrt{1 + \chi(x)} \approx 1 + c\tilde{V}(x)/\omega_p$. Therefore, the \mathcal{PT} symmetry condition $\tilde{V}^*(-\xi) = \tilde{V}(\xi)$ can also be written as $n^*(-\xi) = n(\xi)$.

Here, we would like to make some remarks about the optical potential (14):

- (1) The potential (14) is a nonlinear one, i.e., it depends on the probe-field intensity, $g_1|u|^2$, which is contributed from the Kerr nonlinearity. In general, the coefficient g_1 is a complex number, which, however, can be treated as a real one if the condition $\Delta_3 \gg \Gamma_3$ can be fulfilled. Particularly, the real part of the potential is contributed by the term $g_1|u|^2$ and its symmetry can be *preserved* if the probe-field intensity has an *even* profile in the x direction;
- (2) The imaginary part of the potential is contributed by the term $g_2|v|^2$. In general, the coefficient g_2 is a complex number, which, however, can be treated as a purely imaginary one if the condition $\Delta_1 \approx \Delta_2 \approx 0$ is fulfilled. Further, $|v|^2$ can be made as a constant part

added by an odd function in the x direction (see below), corresponding to a constant loss and a distribution of balanced gain and loss, respectively; (3) The constant loss can be compensated by the additional gain ig_3 , contributed by the incoherent pumping. Thus, the total effect of $g_2|v|^2 + ig_3$ leads to the distribution of balanced gain and loss only, i.e., the imaginary part of the potential is anti-symmetric.

3.2. The Design of \mathcal{PT} Symmetric Potential

Equation (13) is a nonlinear Schrödinger equation (NLSE) with nonlinear optical potential (14). To realize a \mathcal{PT} -symmetric potential, we assume that the far-detuned Stark laser field is composed of a constant part and two Gaussian functions with π -phase difference in the following form

$$v = 5 + 0.1v_0 \left[e^{-\frac{(\xi-\xi_0)^2}{w^2}} - e^{-\frac{(\xi+\xi_0)^2}{w^2}} \right], \quad (15)$$

where $\pm\xi_0$ are center positions of two Gaussian functions and w is the width of each Gaussian pulse. In an experiment, the far-detuned laser field (15) can be prepared in advance by overlapping a constant wave and a pair of Gaussian beams side by side with identical profile and π -phase difference. Moreover, the amplitude of each components can be adjusted according to the demand of symmetry. Finally, the intensity of the far-detuned laser field is

$$\begin{aligned} |v|^2 &= 25 + v_0 \left[e^{-\frac{(\xi-\xi_0)^2}{w^2}} - e^{-\frac{(\xi+\xi_0)^2}{w^2}} \right] + 0.01v_0^2 \left[e^{-\frac{(\xi-\xi_0)^2}{w^2}} - e^{-\frac{(\xi+\xi_0)^2}{w^2}} \right]^2 \\ &\approx 25 + v_0 \left[e^{-\frac{(\xi-\xi_0)^2}{w^2}} - e^{-\frac{(\xi+\xi_0)^2}{w^2}} \right]. \end{aligned} \quad (16)$$

For obtaining the value of coefficients, the system parameters are chosen as $2\gamma_2 = 1 \times 10^3$ Hz, $2\gamma_3 = 36$ MHz, $\omega_p = 2.37 \times 10^{15}$ s $^{-1}$. Other (tunable) parameters are taken as $\kappa_{13} = 3.7 \times 10^{12}$ cm $^{-1}$ s $^{-1}$, $R = 2.5 \times 10^{-3}$ cm, $\Omega_c = 1.65 \times 10^7$ s $^{-1}$, $\Delta_2 = 0$, $\Delta_3 = -1.9 \times 10^9$ s $^{-1}$, $\Omega_{p0} = 3.8 \times 10^5 \sqrt{\sigma}$ s $^{-1}$, $E_{s0} = 2.7 \times 10^4$ V/cm, $\Gamma_{31} = 17$ MHz. Then, we get $L_{\text{diff}} = 1.0$ cm, and

$$g_1 = (1.0 - 0.04i)\sigma, \quad g_2 = 0.02 + 1.0i, \quad g_3 = -25, \quad (17)$$

here, g_1 , g_2 , and g_3 are controlled by Ω_{p0} , E_{s0} , and κ_{13} , respectively. Therefore, the NLSE with the nonlinear optical potential (14) can be further written as

$$i \frac{\partial u}{\partial s} + \frac{\partial^2 u}{\partial \xi^2} + \left\{ \sigma |u|^2 + iv_0 \left[e^{-\frac{(\xi-\xi_0)^2}{w^2}} - e^{-\frac{(\xi+\xi_0)^2}{w^2}} \right] \right\} u = 0. \quad (18)$$

Note that the nonlinear optical potential (the part in the brackets of the last term on the left-hand side of Equation (18)) has the \mathcal{PT} symmetry as long as the probe-field intensity $|u|^2$ has an even profile in the x direction, which can be fulfilled by the fundamental bright soliton solution.

4. EP and Soliton Solutions

Now we discuss the properties of \mathcal{PT} symmetry of Equation (18) with linear and nonlinear potential, respectively. We suppose $u(\xi, s) = u_s(\xi)e^{-i\mu s}$, with μ the propagation constant, then the stable state can be obtained from the following equation

$$-\frac{\partial^2 u_s}{\partial \xi^2} - \left\{ \sigma |u_s|^2 + iv_0 \left[e^{-\frac{(\xi-\xi_0)^2}{w^2}} - e^{-\frac{(\xi+\xi_0)^2}{w^2}} \right] \right\} u_s = \mu u_s. \quad (19)$$

Here, we take $\xi_0 = 2$ and $1/w^2 = 0.45$.

4.1. Property of Linear \mathcal{PT} -Symmetric Potential

When we take $\sigma = 0$, Equation (19) becomes a linear eigenvalue problem. In Figure 3, we show the relationship between the imaginary part of μ and v_0 by searching for the ground state. Since v_0 characterizes the imaginary part of the potential, the breaking of \mathcal{PT} symmetry can occur by changing v_0 . From this figure, it is obvious that the spectrum is entirely real ($\text{Im}(\mu) = 0$) when $v_0 < 0.2$, i.e., the EP locates at $v_0 = 0.2$. Above EP, $v_0 > 0.2$, a phase transition appears and the spectrum becomes partially complex.

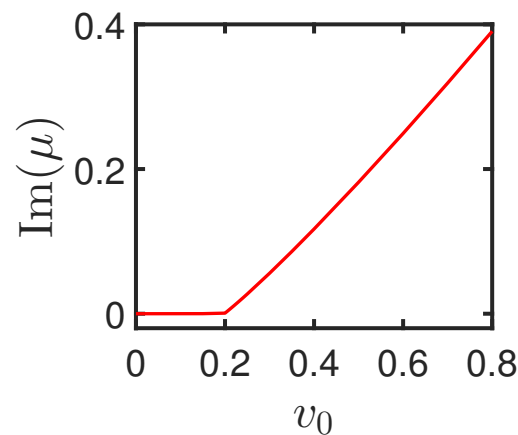


Figure 3. The imaginary part of propagation constant $\text{Im}(\mu)$ as a function of v_0 for $\sigma = 0$.

4.2. Property of Nonlinear \mathcal{PT} -Symmetric Potential

When we take $\sigma = 1$, corresponding to the self-focusing Kerr nonlinearity, Equation (19) becomes a nonlinear ordinary differential equation. In this case, one can only resort to numerical methods for solving this problem. We obtain the stable state solutions corresponding light powers $P = \int_{-\infty}^{+\infty} |\psi|^2 d\xi$ of the probe field by using the Newton conjugate gradient method [25]. Particularly, the probe beam forms a fundamental bright soliton, as shown in the Figure 4. After obtaining the bright soliton solution, $u_s(\xi)$, its stability can be studied by introducing perturbations in the solution, i.e.,

$$u(s, \xi) = \{u_s(\xi) + \epsilon[w_0(\xi)e^{\lambda s} + v_0^*(\xi)e^{\lambda^* s}]\}e^{-i\mu s}, \quad (20)$$

where w_0 and v_0 are perturbation eigenmodes, and λ is the eigenvalue. Substituting Equation (20) into Equation (18), we get the equation

$$i \begin{pmatrix} L_1 & L_2 \\ -L_2^* & -L_1 \end{pmatrix} \begin{pmatrix} w_0 \\ v_0 \end{pmatrix} = \lambda \begin{pmatrix} w_0 \\ v_0 \end{pmatrix}, \quad (21)$$

where $L_1 = \mu + \partial^2/\partial \xi^2 + 2|u_s|^2 + iv_0[e^{-\frac{(\xi-\xi_0)^2}{w^2}} - e^{-\frac{(\xi+\xi_0)^2}{w^2}}]$ and $L_2 = |u_s|^2$. Then, we can use the Fourier collocation method [25] to solve this equation and the soliton $u_s(x)$ is stable if $\lambda \leq 0$ whereas unstable if $\lambda > 0$. The soliton stability can be further confirmed by propagating the soliton solution, directly, by using the split-step Fourier method [25].

Shown in Figure 4 is the fundamental bright soliton and their evolution result. Figure 4a–c illustrate the power P curves as a function of the propagation constant μ with different v_0 . From the results, we find that the solitons only exist in the region of $\mu < 0$, and for each curve there exists the minimum (cut-off value) of the power. In Figure 4d–f, the soliton profiles with different values of v_0 and μ are displayed. Here, the blue solid (red dashed) lines stand for the real (imaginary) part of the soliton. It is obvious that the real part of u_s is an even function about $\xi = 0$, whereas, the imaginary part of u_s is an odd function. The width of soliton is also changed with v_0 and μ .

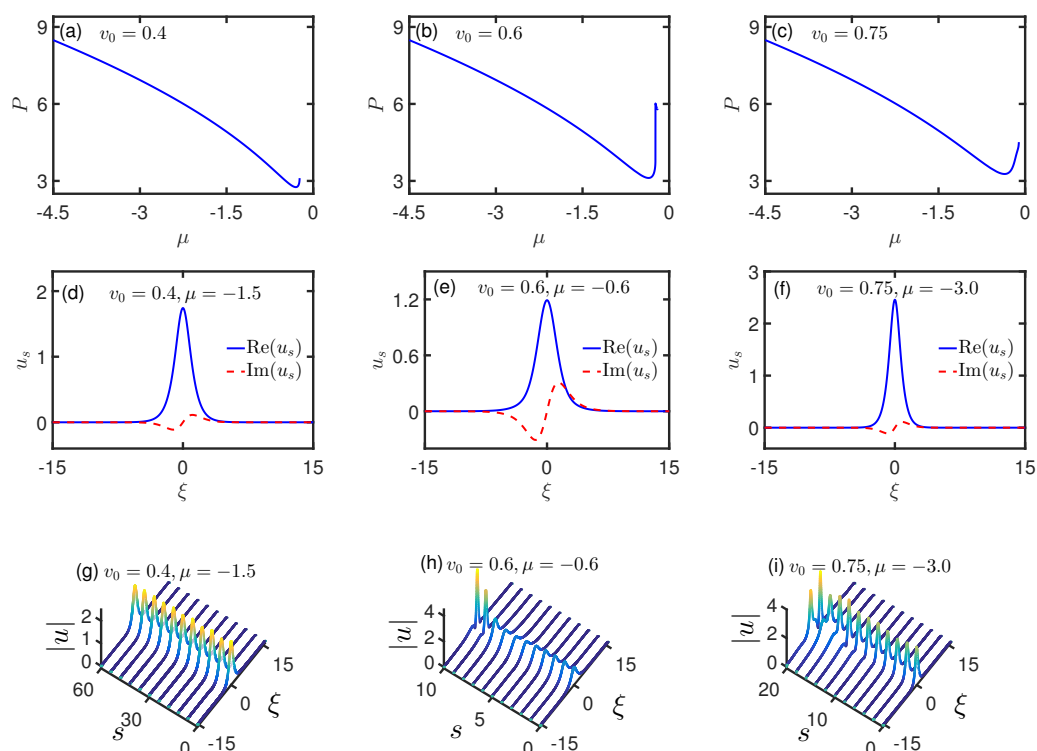


Figure 4. (a–c) Light power curves of fundamental bright solitons as a function of the propagation constant μ with different v_0 . Here, $v_0 = 0.4, 0.6$ and 0.75 , respectively. (d–f) The profiles of bright solitons with different v_0 and the propagation constant μ . Here $(v_0, \mu) = (0.4, -1.5)$, $(0.6, -0.6)$, and $(0.75, -3.0)$ in panels (d–f), respectively. The blue solid lines denote the real parts of solitons, and the red dashed lines denote the imaginary parts of solitons. (g–i) The evolution results of bright solitons with different v_0 and μ . Here $(v_0, \mu) = (0.4, -1.5)$, $(0.6, -0.6)$, and $(0.75, -3.0)$ in panels (g–i), respectively.

The soliton stability is further confirmed by a direct simulation of Equation (18) by taking the soliton solution as the initial condition, after adding a random perturbations into the initial condition of evolution. To this end, the initial value is taken as $u(s = 0, \xi) = u_s(\xi)(1 + \varepsilon f_1)$, where $\varepsilon = 0.05$ and f_1 is a random function uniformly distributed in the interval $[0, 1]$. The evolution results of solitons in Figure 4d–f are shown in Figure 4g–i, respectively. With increasing the propagation distance s , we see that the soliton in Figure 4d propagates stably as shown in Figure 4g. However, in Figure 4h, the soliton with $v_0 = 0.6$, $\mu = -0.6$ experiences a collapse with increasing s , which is unstable. Finally, in Figure 4i, the soliton splits with the increase of s , which is unstable, either.

In order to have a full picture of the existence and stability of the fundamental bright solitons, we calculate the existence and stability regions of solitons in Figure 5a. The region below the blue dashed line denotes that the solitons can be generated in the parameter intervals, we find that μ does not change much by changing v_0 , namely, the imaginary part of \mathcal{PT} -symmetric potential has little effect on the generation of solitons. Furthermore, we are interested in the stability of solitons. Due to the self-focusing Kerr nonlinearity ($\sigma = 1$), the fundamental bright solitons are stable in the region on the left of the red solid line, as shown in Figure 5a. Therefore, every points on the red solid line can be treated as an EP for the nonlinear \mathcal{PT} -symmetric potential. Compared with the linear case, for each value of μ , the value of v_0 is larger than 0.2 . Thus, we conclude that the self-focusing Kerr nonlinearity can delay the occurrence of the \mathcal{PT} symmetry breaking, which also triggers the instability of solitons. Particularly, we see that stable solitons can exist for $v_0 = 0.8$ marked by the blue pentagram.

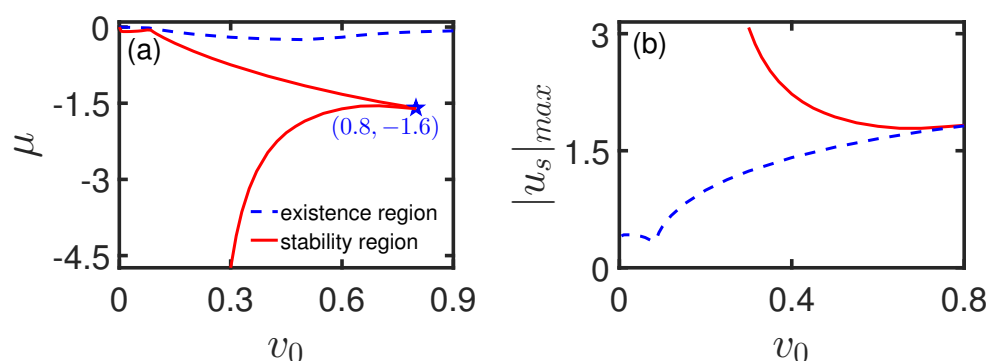


Figure 5. (a) The existence region and stable region of solitons as the functions of v_0 and the propagation constant μ . It is the existence region of the bright solitons under the blue dashed line, and it is the stability region of bright solitons on the left of red solid line. The blue pentagram denotes the coordinate of point $(0.8, -1.6)$. (b) The maximum amplitude $|u_s|_{\max}$ of solitons as a function of v_0 . The solitons are obtained by taking the parameters along the red solid line in the panel (a). In the red solid line, μ changes from -4.74 to -1.6 , and it changes from 0 to -1.16 along the blue dashed line.

Shown in Figure 5b is the maximum amplitude $|u_s|_{\max}$ of solitons as a function of v_0 . The solitons are obtained by taking the parameters along the red solid line in Figure 5a. Therefore, the curve in this figure tells us the relation between the EP location and maximum amplitude of solitons. From this figure, we find that with the increase of the maximum amplitude, the EP location increases firstly (denoted by the blue dashed line), and then decreases (denoted by the red solid line). The reason behind this behavior is that the soliton profiles change with the increase of maximum amplitude, that is, the shape of the real part of the \mathcal{PT} -symmetric potential is not fixed. Thus, it is possible to control the location of EP by changing the soliton amplitude, which provides new a method for controlling EP.

5. Conclusions

In conclusion, we have proposed a scheme to realize a nonlinear \mathcal{PT} symmetric optical potential in a coherent atomic gas. The system under study consists of a cold three-level atomic media driven by two lasers, works under the condition of EIT. We showed that it is possible to construct an optical potential with \mathcal{PT} symmetry due to the interplay between the Kerr nonlinearity, the linear Stark potential, and the optical gain. Because the real part of the \mathcal{PT} -symmetric potential depends only on the intensity of the probe field, the potential is nonlinear and its \mathcal{PT} -symmetric properties are determined by the input laser intensity of the probe field. Moreover, we obtained the fundamental soliton solutions of the system and attained their stability region in the system parameter space. The location of EPs on the soliton maximum amplitude is also illustrated. The research results reported here is not only useful for understanding the unique properties of \mathcal{PT} symmetry of a nonlinear optical potential, but also promising for designing novel optical devices applicable in optical information processing and transmission.

Author Contributions: Conceptualization, H.L. and J.L.; methodology, D.A.P.A.; software, J.D. and G.Z.; validation, D.A.P.A. and G.Z.; data curation, D.A.P.A. and J.D.; writing—original draft preparation, H.L.; writing—review and editing, H.L.; project administration, H.L. and J.L. All authors have read and agreed to the published version of the manuscript.

Funding: This work was funded by the National Natural Science Foundation of China (Grant No. 12074343, No. 11835011), Natural Science Foundation of Zhejiang Province of China (Grant No. LZ22A050002).

Institutional Review Board Statement: Not applicable.

Informed Consent Statement: Not applicable.

Data Availability Statement: Not applicable.

Conflicts of Interest: The authors declare no conflict of interest.

Appendix A. Explicit Expression of Equation (3)

Equations of motion for ρ_{ij} are given by

$$i\frac{\partial}{\partial t}\rho_{11} + i\Gamma_{31}\rho_{11} - i\Gamma_{13}\rho_{33} + \Omega_p^*\rho_{31} - \Omega_p\rho_{31}^* = 0, \quad (A1)$$

$$i\frac{\partial}{\partial t}\rho_{22} - i\Gamma_{23}\rho_{33} + \Omega_c^*\rho_{32} - \Omega_c\rho_{32}^* = 0, \quad (A2)$$

$$i\left(\frac{\partial}{\partial t} + \Gamma_3\right)\rho_{33} - i\Gamma_{31}\rho_{11} - \Omega_p^*\rho_{31} + \Omega_p\rho_{31}^* - \Omega_c^*\rho_{32} + \Omega_c\rho_{32}^* = 0, \quad (A3)$$

$$\left(i\frac{\partial}{\partial t} + d_{21}\right)\rho_{21} + \Omega_c^*\rho_{31} - \Omega_p\rho_{32}^* = 0, \quad (A4)$$

$$\left(i\frac{\partial}{\partial t} + d_{31}\right)\rho_{31} + \Omega_p(\rho_{11} - \rho_{33}) + \Omega_c\rho_{21} = 0, \quad (A5)$$

$$\left(i\frac{\partial}{\partial t} + d_{32}\right)\rho_{32} + \Omega_c(\rho_{22} - \rho_{33}) + \Omega_p\rho_{21}^* = 0, \quad (A6)$$

with $d_{jl} = \Delta'_j - \Delta'_l + i\gamma_{jl}$.

Appendix B. Perturbation Expansion of the MB Equations

The coefficients of perturbation expansion are given by

$$\alpha_{21}^{(1)} = -\frac{d_{31}^{(0)}(\rho_{32}^{(0)})^* + \Omega_c^*(\rho_{11}^{(0)} - \rho_{33}^{(0)})}{D_1}, \quad (A7)$$

$$\alpha_{31}^{(1)} = \frac{K}{\kappa_{13}}.$$

$$\begin{aligned} \alpha_{11}^{(2)} &= \{2\Gamma_{13}\text{Im}(\Omega_c d_{32}^{(0)} \alpha_{21}^{(1)}) - 2\text{Im}(\alpha_{31}^{(1)})[\Gamma_{23}|d_{32}^{(0)}|^2 + 4\gamma_{32}|\Omega_c|^2]\}/D_0, \\ \alpha_{22}^{(2)} &= \{-2(\Gamma_{13} + \Gamma_{31})\text{Im}(\Omega_c d_{32}^{(0)} \alpha_{21}^{(1)}) + 2\text{Im}(\alpha_{31}^{(1)})[\Gamma_{23}|d_{32}^{(0)}|^2 + 2\gamma_{32}|\Omega_c|^2]\}/D_0, \\ \alpha_{32}^{(2)} &= [2(\Gamma_{13} + 2\Gamma_{31})|\Omega_c|^2\text{Im}(\alpha_{21}^{(1)}) - \Gamma_{31}\Gamma_{23}(d_{32}^{(0)} \alpha_{21}^{(1)})^* - 2\Gamma_{23}(d_{32}^{(0)})^* \Omega_c \text{Im}(\alpha_{31}^{(1)})]/D_0, \\ \alpha_{33}^{(2)} &= \{2\Gamma_{31}\text{Im}(\Omega_c d_{32}^{(0)} \alpha_{21}^{(1)}) + 4\gamma_{32}\text{Im}(\alpha_{31}^{(1)})|\Omega_c|^2\}/D_0. \end{aligned} \quad (A8)$$

References

- Bender, C.M. Making sense of non-Hermitian Hamiltonians. *Rep. Prog. Phys.* **2008**, *70*, 947–1018. [\[CrossRef\]](#)
- Makris, K.G.; El-Ganainy, R.; Christodoulides, D.N.; Musslimani, Z.H. \mathcal{PT} symmetric periodic optical potentials. *Int. J. Theor. Phys.* **2011**, *50*, 1019–1041. [\[CrossRef\]](#)
- Bittner, S.; Dietz, B.; Günther, U.; Harney, H.L.; Miski-Oglu, M.; Richter, A.; Schäfer, F. \mathcal{PT} symmetry and spontaneous symmetry breaking in a microwave billiard. *Phys. Rev. Lett.* **2012**, *108*, 024101. [\[CrossRef\]](#)
- Rüter, C.E.; Makris, K.R.; El-Ganainy, R.; Christodoulides, D.N.; Segev, M.; Kip, D. Observation of parity-time symmetry in optics. *Nat. Phys.* **2010**, *6*, 192–195. [\[CrossRef\]](#)
- Regensburger, A.; Bersch, C.; Miri, M.-A.; Onishchukov, G.; Christodoulides, D.N.; Peschel, U. Parity-time synthetic photonic lattices. *Nature* **2012**, *488*, 167–171. [\[CrossRef\]](#)
- Feng, L.; Xu, Y.-L.; Fegadolli, W.S.; Lu, M.-H.; Oliveira, J.E.B.; Almeida, V.R.; Chen, Y.-F.; Scherer, A. Experimental demonstration of a unidirectional reflectionless parity-time metamaterial at optical frequencies. *Nat. Mat.* **2013**, *12*, 108–113. [\[CrossRef\]](#)
- Peng, B.; Özdemir, S.K.; Lei, F.; Monifi, F.; Gianfreda, M.; Long, G.L.; Fan, S.; Nori, F.; Bender, C.M.; Yang, L. Parity-time-symmetric whispering-gallery microcavities. *Nat. Phys.* **2014**, *10*, 394. [\[CrossRef\]](#)
- Chang, L.; Jiang, X.; Hua, S.; Yang, C.; Wen, J.; Jiang, L.; Li, G.; Wang, G.; Xiao, M. Parity-time symmetry and variable optical isolation in active-passive-coupled microresonators. *Nat. Photon.* **2014**, *8*, 524. [\[CrossRef\]](#)
- Guo, A.; Salamo, G.J.; Duchesne, D.; Morandotti, R.; Volatier-Ravat M.; Aimez, V.; Sililoglou, G.A.; Christodoulides, D.N. Observation of \mathcal{PT} -symmetry breaking in complex optical potentials. *Phys. Rev. Lett.* **2009**, *103*, 093902. [\[CrossRef\]](#)

10. Sun, Y.; Tan, W.; Li, H.; Li, J.; Chen, H. Experimental demonstration of a coherent perfect absorber with \mathcal{PT} phase transition. *Phys. Rev. Lett.* **2014**, *112*, 143903. [[CrossRef](#)]
11. Lawrence, M.; Xu, N.; Zhang, X.; Cong, L.; Han, J.; Zhang, W.; Zhang, S. Manifestation of \mathcal{PT} symmetry breaking in polarization space with terahertz metasurfaces. *Phys. Rev. Lett.* **2014**, *113*, 093901. [[CrossRef](#)]
12. Benisty, H.; Degiron, A.; Lupu, A.; De Lustrac, A.; Cheñais, S.; Forget, S.; Besbes, M.; Barbillon, G.; Bruyant, A.; Blaize, S.; et al. Implementation of \mathcal{PT} symmetric devices using plasmonics: Principle and applications. *Opt. Express* **2011**, *19*, 18004–18019. [[CrossRef](#)]
13. Schindler, J.; Li, A.; Zheng, M.C.; Ellis, F.M.; Kottos, T. Experimental study of active LRC circuits with \mathcal{PT} symmetries. *Phys. Rev. A* **2011**, *84*, 040101(R). [[CrossRef](#)]
14. Lin, Z.; Ramezani, H.; Eichelkraut, T.; Kottos, T.; Cao, H.; Christodoulides, D.N. Unidirectional invisibility induced by \mathcal{PT} -symmetric periodic structures. *Phys. Rev. Lett.* **2011**, *106*, 213901. [[CrossRef](#)]
15. Feng, L.; Wong, Z.J.; Ma, R.; Wang, Y.; Zhang, X. Single-mode laser by parity-time symmetry breaking. *Science* **2014**, *346*, 972. [[CrossRef](#)]
16. Hodaie, H.; Miri, M.; Heinrich, M.; Christodoulides, D.N.; Khajavikhan, M. Parity-time-symmetric microring laser. *Science* **2014**, *346*, 975. [[CrossRef](#)]
17. Hodaie, H.; Hassan, A.U.; Wittek, S.; Garcia-Gracia, H.; El-Ganainy, R.; Christodoulides, D.N.; Khajavikhan, M. Enhanced sensitivity at higher-order exceptional points. *Nature* **2017**, *548*, 187. [[CrossRef](#)]
18. Chen, W.; Özdemir, Ş.K.; Zhao, G.; Wiersig, J.; Yang, L. Exceptional points enhance sensing in an optical microcavity. *Nature* **2017**, *548*, 192. [[CrossRef](#)]
19. Hang, C.; Huang, G.; Konotop, V.V. \mathcal{PT} symmetry with a system of three-level atoms. *Phys. Rev. Lett.* **2013**, *110*, 083604. [[CrossRef](#)]
20. Sheng, J.; Miri, M.; Christodoulides, D.N.; Xiao, M. \mathcal{PT} -symmetric optical potentials in a coherent atomic medium. *Phys. Rev. A* **2013**, *88*, 041803(R). [[CrossRef](#)]
21. Li, H.; Dou, J.; Huang, G. \mathcal{PT} symmetry via electromagnetically induced transparency. *Opt. Express* **2013**, *21*, 320503. [[CrossRef](#)]
22. Demtröder, W. *Laser Spectroscopy: Basic Concepts and Instrumentation*, 3rd ed.; Springer: Berlin, Germany, 2003; Chapter 10.
23. Huang, G.; Deng, L.; Payne, M.G. Dynamics of ultraslow optical solitons in a cold three-state atomic system. *Phys. Rev. E* **2005**, *72*, 016617. [[CrossRef](#)]
24. Li, H.-j.; Wu, Y.-p.; Huang, G. Stable weak-light ultraslow spatiotemporal solitons via atomic coherence. *Phys. Rev. A* **2011**, *84*, 033816. [[CrossRef](#)]
25. Yang, J. Numerical methods for nonlinear wave equations. In *Nonlinear Waves in Integrable and Nonintegrable Systems*; Haberman, R., Ed.; SIAM: Philadelphia, PA, USA, 2011; Chapter 7.